Jet stability and wall impingement flow field in a thermal striping experiment

S. Lomperski, A. Obabko, E. Merzari, P. Fischer, W. D. Pointer*
Argonne National Laboratory, 9700 S. Cass Ave., Argonne IL, USA
*Oak Ridge National Laboratory, P.O. Box 2008, Oak Ridge, TN 37831

We present velocity and temperature field measurements for a 0.9 x 0.9 x 1.7 m glass tank in which two air jets at Re=10000 mix and impinge upon the lid at ambient temperature and pressure. Flow patterns are characterized across a 350 x 200 mm plane located 3 mm below the lid for two inlet geometries: 1) "extended", in which inlet channels protrude above the tank base, and 2) "flush", a flat base without protrusions. This minor geometry variation produced distinct changes in the lid flow field, appearing as three stagnant regions for the extended case and only one for flush. The dichotomy is attributed to system stability characteristics: jets are stable in the extended case and unstable for flush. In a separate set of nonisothermal tests, the impingement temperature field was measured for inlet temperature mismatches of 4 ^{o}C and jets near Re=10000. A 50 m-long fiber optic distributed temperature sensor positioned 2 mm below the lid measured at 1350 locations. Like the velocity fields, the temperature fields differ for the two inlet geometries: good thermal mixing for the flush case and subdued mixing for the extended case.

Simulations with the spectral element code Nek5000 replicated the observed stability dichotomy, duplicating the number of stagnant regions observed in the experiment and matching their locations within ±10 mm. Simulation data suggests that flush case instability is due to interactions between jets and wall flows at the bottom of the tank. The clear flow dichotomy exhibited by this two-jet setup presents an unambiguous case to test the ability of CFD tools to predict subtle flow field changes driven by minor modifications in geometry in the context of thermal striping.

Keywords: CFD validation, experiment, thermal striping, Nek5000, PIV, fiber optic distributed temperature sensor, jet impingement

Highlights

Measured wall impingement velocity and temperature fields in a jet mixing experiment

A small change in inlet geometry toggled jets from stable to unstable and altered impingement fields

The spectral element code Nek5000 reproduced observed stability dichotomy

Introduction

Electric power plants rely upon piping systems to transport and sometimes mix hot and cold fluid streams. Mixing may generate local fluctuations in fluid temperature that can be transferred to the piping itself to produce thermal cycling and thermal stresses. Cycling may be random or periodic, but in either case it can progressively weaken materials through the process of thermal fatigue. High-cycle thermal fatigue has been observed in boiler tubes [1] a steam exhaust silencer [2] and mixing tees of nuclear power stations [3,4]. Even modest thermal cycling can critically weaken materials over the decades-long life of a power plant.

The term 'thermal striping' is often used for the collective phenomena of fluctuating fluid temperature, thermal cycling of structures, and associated stresses. Some also include the mechanical fatigue induced by protracted cycling. Thermal striping can occur in regions of thermal stratification [5], but this paper concerns convective mixing as the source of thermal cycling.

Thermal striping is of special concern for liquid metal-cooled nuclear fast reactors. Fluctuations in fluid temperature are readily transferred to piping components due to the low Prandtl number of liquid metals. Fluctuations can be substantial because of potentially high ΔT between mixing flow streams, in some instances >100 ^{o}C. For example, weld failures in sodium fast reactors have been associated with thermal striping [6]. A general sense of the many potential sources of thermal striping in fast reactors is available in [7,8].

A variety of thermal mixing experiments have been conducted in the context of thermal striping. Of particular interest are those employing liquid sodium since it is the working fluid of the most established class of fast

reactor. Hot and cold concentric sodium jets have been mixed in tanks with measurements of the temperature field for comparison with air and water systems to characterize similarity relations [9,10]. Kimura et. al. [11] examined heat transfer between a wall and three rectangular jets with the central one colder than the outer two. Temperature fluctuations in both fluid and wall were measured to characterize transient heat transfer. Simoneau et al. [12] studied mixing of hot and cold flows at a 90° branch connection and measured downstream temperatures for comparison with simulations. Concerns over thermal striping at tee-junctions have motivated design of special components to enhance mixing. A multi-jet tee-mixing device was tested in sodium for analysis of thermal loading and component stresses [13]. Thermal mixing efficiencies and thermal loading of structures are also of interest in applications employing heavy liquid metals [14].

Sodium experiments provide considerable insight into thermal striping mechanisms but are of limited utility for CFD (computational fluid dynamics) code validation. Validation generally involves comparisons between simulated and measured velocity fields, but the opacity of sodium precludes high-fidelity velocity mapping with standard optical measurement techniques like PIV (particle image velocimetry). Likewise, optical temperature mapping techniques like LIF (laser-induced fluorescence) are unsuitable for sodium. As a result, transparent fluids such as air or water are used in lieu of sodium when the data is intended for rigorous CFD benchmarking. There is a remarkably extensive body of experimental work on jet mixing, much of it employing optical instruments for CFD validation. We note here only some representative studies conducted in the context of thermal striping for nuclear engineering applications along with recent work devoted to high-resolution characterization of jet impingement flow fields that include heat transfer measurements.

As a recognized locus for thermal striping, the mixing tee-junction is a commonly studied geometry in the field of nuclear engineering. Water is often the working fluid and the flow field downstream of the branch is mapped with PIV. Kimura et. al. [15] characterized jet impingement and mixing between a hot stream and a smaller cold branch flow while Hosseini et. al. [16] examined flow fields in a similar geometry under isothermal conditions. Others have characterized mixing using LIF [17] or wire mesh sensors [18,19]. Thermal striping in tee-junction geometries continues to be of interest in the nuclear field, but the current work addresses mixing above a reactor core and is more closely related to jet mixing.

A number of water jet mixing studies have been conducted with fast reactor thermal striping in mind. Jets have been mixed within tanks and the flow fields characterized by PIV [20] ultrasound Doppler velocimetry [21] and laser Doppler velocimetry [22]. Rathee et al. [23] used both PIV and a shadowgraph visualization technique to characterize the impingement flow field of two differentially heated water jets, testing a range of inlet velocity ratios.

Of special interest here are jet-impingement studies involving measurements of both velocity and temperature fields. Typical setups direct a single air jet at a heated plate while measuring velocity fields and plate Nusselt number [e.g., 24-29]. Less common are multiple-jet setups such as that of Fanning et al. [30], who examined interactions between two adjacent jets, and the nine-jet setup of Mehryar and Giovanni [31]. Though these studies involve sophisticated field measurements in thermal striping-like configurations, they generally focus on heat transfer efficiencies rather than stability and its effect on the impingement fields, and they do not involve geometries like those of fast reactor subchannels.

This paper describes a jet mixing experiment with wall impingement in a geometry patterned off the upper plenum of a sodium fast reactor. It mimics situations where temperature mismatches in core assembly outlet flows impinge upon structures and induce thermal cycling. The working fluid is air rather than sodium to accommodate optical instrumentation. Air is not commonly chosen for thermal striping studies in part because flow seeding for PIV can be problematic, but it could be considered a superior working fluid for such work. Jet mixing behavior is governed by the Reynolds and Peclet numbers, where Pe=RePr and Pr is the Prandtl number. The Prandtl number for sodium at reactor temperature (~0.005) is closer to that of air near room temperature (~0.7) than water (~7). If one matches Reynolds numbers of the model and sodium prototype, the Peclet number is better matched with air than water by roughly a factor of ten. It is recognized that the Prandtl number of air is far too low for thermal boundary layer similarity in fluid/structure heat transfer [32]. But air is a suitable surrogate for thermal mixing investigations [9,10] while sodium can be used to address specific issues where fluid/structure heat transfer is the central concern.

We present measurements of wall impingement velocity and temperature fields for two test section configurations with differing inlet geometries. The two cases exhibit markedly different lid flow fields that indicate jet stability in one configuration and instability in the other. Measurements are compared to simulations with Nek5000, a spectral element method code. Though thermal striping ultimately concerns structural stresses rather

than flow fields, the current work is relevant since root causes lie in fluid dynamics and heat transfer phenomena. This study is intended to support CFD code validation in the context of thermal striping. Reliable simulation capability is especially important in the design of advanced reactors since prototype testing is costly.

2. Experiment

A glass tank 0.94 x 0.94 x 1.73 m long serves as the test section for two air jets that enter through the base at atmospheric pressure and ambient temperature (Fig. 1). They impinge upon the lid and mix before exiting through a filtered vent on top of the tank. The pressure drop across the vent is ~50 Pa. Tank walls are made of 6 mm thick soda-lime glass plate. The base and lid were fabricated from 12 mm thick aluminum plates. The inlet channels are hexagonal aluminum ducts 136 mm flat-to-flat, cross sectional area 0.016 m^2, wetted perimeter 0.47 m, and length 2.7 m. The hexagonal shape is typical of sodium reactor core subchannels and profile dimensions match those proposed for an early design of a U.S. advanced burner test reactor.

The tank lid is the focal point of the experiment since it serves as the structure in the thermal striping scenario. A transparent polycarbonate window, 920 x 778 mm and 12 mm thick, sits directly above the inlets to accommodate PIV measurements of the impingement flow field. The flow field was measured for two different configurations: one is termed "extended", in which the hexagonal channels protrude 136 mm into the tank as shown in Fig. 2. The second configuration lacks the penetrations and is designated "flush". Extensions are cut from the same stock as the fixed channels and sit without glue or fittings to ease switches between the two configurations. Flow is conditioned by a series of meshes and honeycomb flow straighteners. Additional details can be found in [33].

2.1 Instrumentation

The light source for the PIV system is a Litron LDY304 Nd:YLF dual cavity pulsed laser used in single cavity mode to avoid measurement uncertainties associated with misalignment of two beams. Pulse power was 30 mJ and light sheet thickness approximately 2 mm, positioned ~3 mm from the underside of the lid as shown in Fig. 2. Estimated uncertainty in light sheet distance from the lid is ±1 mm.

The camera is an IDT Y7 with a 1920 x 1080 array of 7.24 x 7.24 µm pixels fitted with a 50 mm Navitar lens used at an aperture of 0.96 and typical field of view of 350 x 200 mm. Image pairs with a Δt of 1 ms were recorded at 5 Hz. IDT's Motion Studio was used for both laser and camera triggering and image capture. Analysis was performed with Dantec's Dynamic Studio using adaptive correlation with 32 x 32 pixel interrogation areas (5.8 x 5.8 mm) with 50% overlap and a subpixel refinement option. Vector fields were not filtered, but range validation was used to eliminate physically unrealistic data. Velocity accuracy is approximately 0.03 m/s based on comparisons with hot wire anemometer measurements, which were made on two different days to confirm repeatability. One

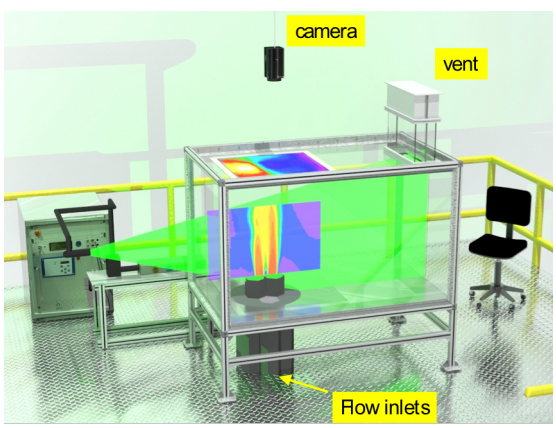

Fig. 1. Jet mixing experiment for thermal striping; jet velocities indicated by scalar contour within laser light sheet at tank midplane; contour on lid represents temperature for the case of one heated jet.

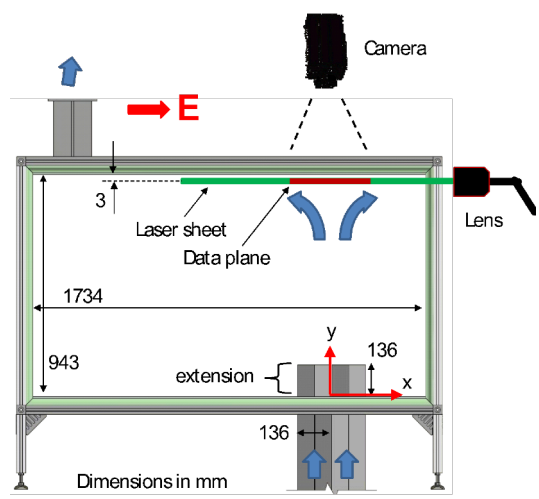

Fig. 2. Instrumentation layout for lid velocity measurements with PIV, extended case shown.

data set is included in Fig. 5 along with the PIV measurements of inlet boundary conditions. Discrepancies between hot wire and PIV data are highest near jet edges where velocity gradients are highest. This is associated with probe positioning uncertainties that lead to spatial mismatches between hot wire and PIV data. Positioning errors are most consequential where velocity gradients are highest.

Capturing the entire impingement field of interest required a relatively large PIV field of view, which leads to peak locking errors in the RMS readings [34]. Time-averaged velocities are unaffected, but RMS is overestimated roughly 0.02 m/s in the main flow over the inlets. PIV accuracy in the lid region was not checked with the hot wire probe, but the setup is similar to the one used for the inlets and so errors are expected to be similar. High measurement precision is not critical in this particular study since its focus is characterizing flow field patterns. Accuracy and repeatability of the boundary conditions are more important.

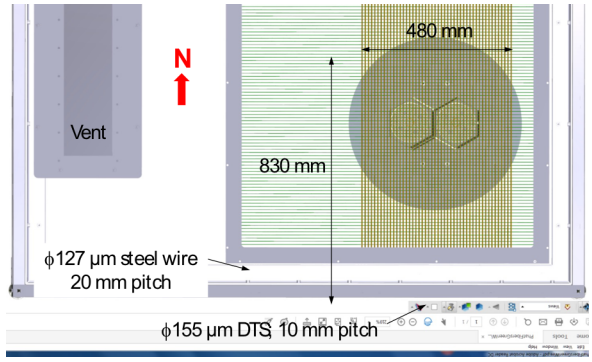

Fig. 3. Top view of mounting configuration for DTS located 3 mm below lid. A single 50 m-long sensor makes 49 passes between tank walls.

Inlet and vent temperatures were measured using K-type TCs with an accuracy of ±2.2 ^{o}C for absolute temperature and ±0.1 ^{o}C for ΔT. The ΔT between the inlets is known to within ±0.1 ^{o}C. Flow was measured by a combination of E&H Promass 83F Coriolis flow meters and Teledyne 301 thermal mass flow meters with the former responsible for more than 97% of the flow and the latter dedicated only to the PIV seeding flow. Coriolis meter accuracy is ±0.8% for Reynolds 10000 and ±0.4% at Reynolds 18000.

Flow was seeded with a polyethylene glycol mist at an average droplet diameter of ~2 µm. Mist was introduced at the bottom end of the flow channels, 2.7 m from the tank, generating a particularly homogenous seeding density. Mist flow rate to each channel was ~35 slpm measured with an accuracy of ±0.4 slpm.

Air temperature below the lid was measured with a fiber optic distributed temperature sensor (DTS) located 3 mm below the lid (1 mm above the PIV plane), but installed after the tests with PIV. Figure 3 shows the mounting configuration for the 50 m sensor made of commercial telecom optical fiber (ϕ155 µm polyimide-coated single-mode Specialty Photonics CL POLY 1310). It was supported by ϕ127 µm steel wire strung across the long axis of the tank with a 20 mm pitch. The DTS was woven between the wires in an alternating pattern and wound back and forth across the short axis of the tank 49 times. The setup generated 1350 data points across a 0.5 x 0.8 m plane.

The sensing system for the DTS is an ODiSI (Optical Distributed Sensor Interrogator) model A50 interrogator from Luna Inc. based on Rayleigh scattering. It was configured for temperature resolution of 0.1 ^{o}C and logging rate of 4 Hz. The system supports spatial resolution down to 10 mm, but 30 mm resolution was used instead to reduce signal noise. The sensing technique is outlined in [35,36] while the particular sensor layout used here is described in more detail in [37].

2.2 Boundary conditions

The velocity field directly above the inlets was mapped with PIV across seven north/south planes and five east/west planes. Figure 4 shows locations of the E/W planes, which were line-sampled to generate the charts in Fig. 5. Sample lines are 15 mm above the inlets, i.e., y=15 mm for the flush case and y=151 mm for the extended case. The curves indicate the vertical component of the velocity vector. The flush case profiles are more irregular than those of the extended case and also visibly less symmetric around the centerline (z=0). Flush case asymmetries include dips into negative velocity near the gap between inlets (inside edges are 9 mm apart). Asymmetries are a sign of jet skewing westward towards the vent. In contrast, jets in the extended case are upright (not skewed) and velocity at x=0 is near zero for both the centerline and ±38 mm curves.

The discrepancy between the two cases demonstrates the disadvantage of characterizing inlet boundary conditions with measurements inside the tank, which is part of the validation domain. Ideally, mapping would be far upstream of the inlets where flow fields are identical in each case, but such a setup was beyond the scope of this work. Note, however, that our simulations reproduced observed jet stability dichotomies with differing Reynolds

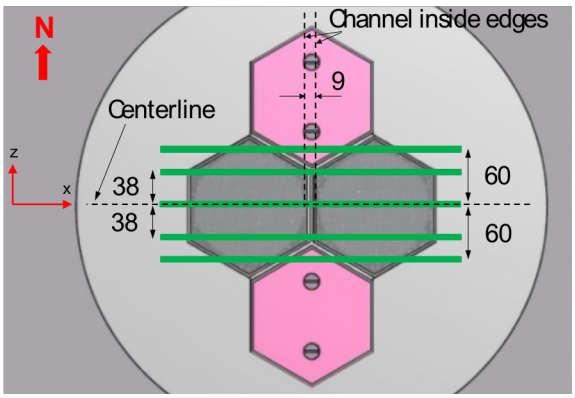

Fig. 4. Top view of PIV measurement planes for inlet velocity characterization.

numbers and treatments of inlet turbulence. Thus these tests are of potential interest for validation in part because global behavior is sensitive to the geometry change rather than details of the inlet velocity and turbulence fields, which are often challenging to characterize in acceptable detail and accuracy.

3. Test results

Results are presented as a series of contour plots to illustrate the dependence of lid flow field on inlet geometry beginning with isothermal matched flows at Re=10000. It will be seen that flow field patterns are distinctly different for the two cases. The data suggests that the jets are stable in the extended case but unstable in the flush case. Results for mismatched inlet flow rates and temperatures follow. These supplementary tests demonstrate that the stability dichotomy is not restricted to precisely matched flows. For the range of inlet conditions tested, inlet geometry alone governs jet stability.

3.1 PIV: matched isothermal jets

Figure 6a presents flow velocity across the lid plotted as velocity magnitude $V_{mag}=\sqrt{u^2+v^2}$ based on 1000 measurements recorded at 5 Hz over 200 s. Profiles of the hexagonal channels are overlaid onto the contours as an orientation aid. The viewpoint is above the tank looking down onto the lid with the outlet at the northwest corner to match orientation of the schematics. The coordinate system origin is centered between the two inlets at the tank centerline with velocity components towards the north and east defined as positive. Cardinal points are used here as a convenience that simplifies plot descriptions in the text. The east tank wall is at +434 mm and the west wall at -1300 mm.

The black spots in Fig. 6a mark regions where the time-averaged velocity is near zero. These are denoted as "stagnant" regions for brevity even though instantaneous velocity is generally nonzero. Considered in this fashion, the extended case exhibits three stagnant regions and the flush case only one.

Distinctions between the two cases are highlighted by decomposing velocity into east/west and

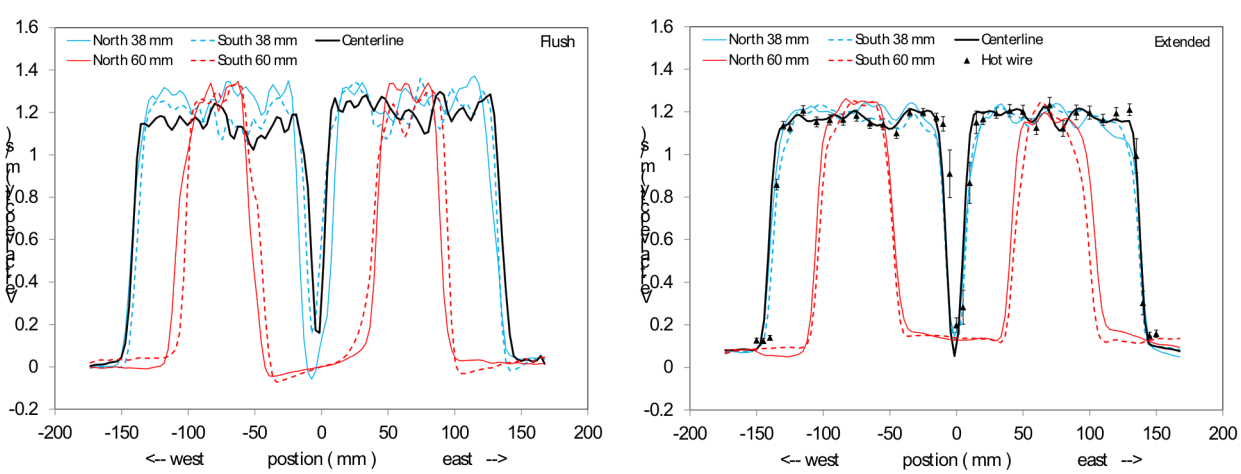

Fig. 5. Inlet velocities sampled from the data planes of Fig. 4. Sample lines located 15 mm above inlet, i.e., y=15 mm for flush case and y=151 mm for extended case. Error bars for hot wire data indicate ±σ.

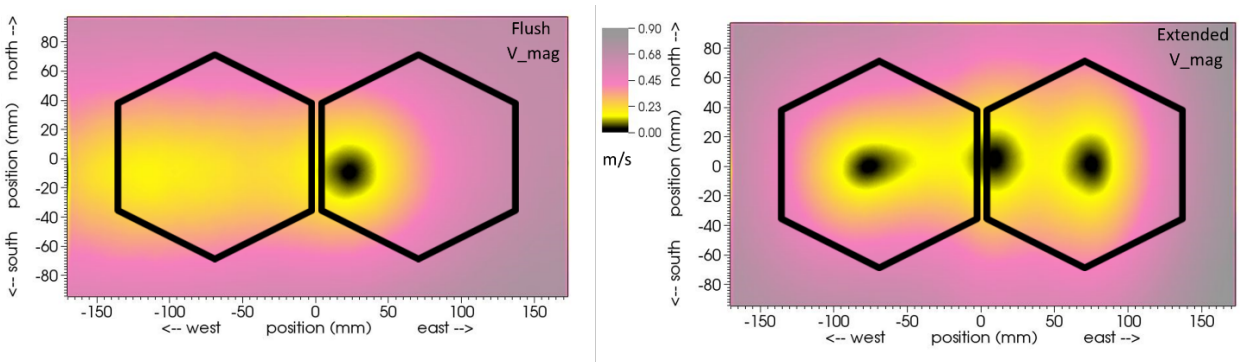

a) Velocity magnitude $V_{mag} = \sqrt{u^2 + v^2}$

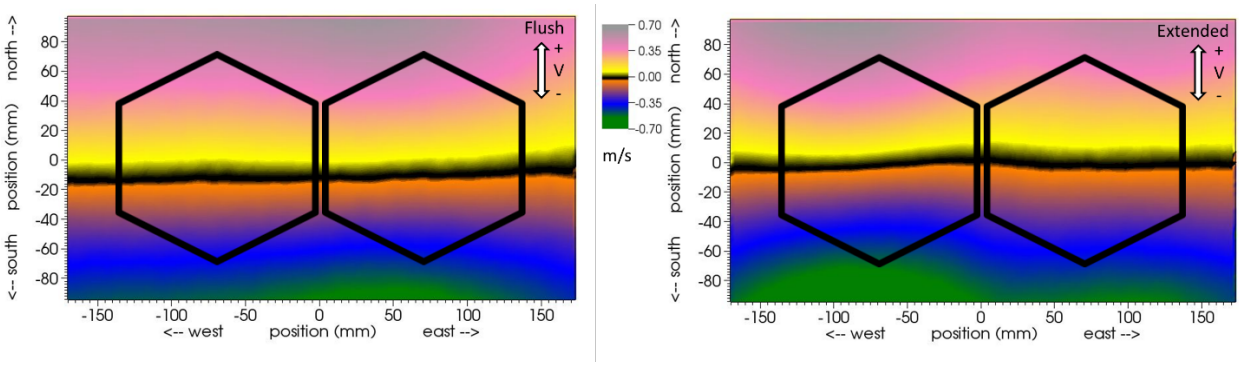

b) N/S velocity component

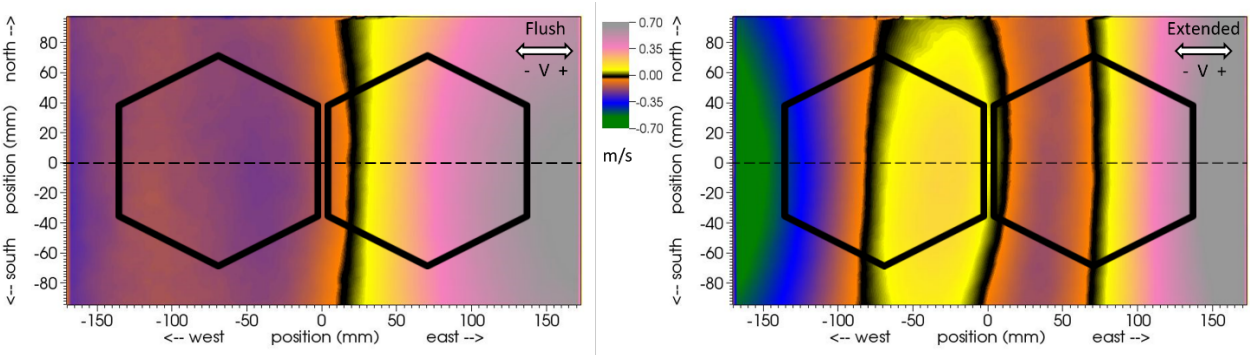

c) East/west velocity component; dashes show location of sampling line used to generate curves in Figs. 8 & 9.

Fig. 6. Time-averaged velocity 3 mm below lid for matched inlet flows at Reynolds 10000 and ambient temperature. Averages based on 1000 frame pairs logged at 5 Hz for 200 s. Top view looking down on lid with silhouettes of hexagonal inlets included as an orientation aid. Black indicates zero velocity in all plots.

north/south components. The N/S components (Fig. 6b) are similar, both having a stagnant band over the inlets that is nearly parallel to the tank's E/W axis. Each band marks the region where the jets split into northward and southward flows that travel across the lid towards opposing walls. Neither case displays exceptional symmetry, but recall that the outlet is located off-axis and so genuine symmetry is not expected. Indeed, the vent was intentionally positioned off-axis to avoid symmetries that could cause random cycling of the flow field between mirror-image states.

Unlike the N/S velocity component, the E/W component differs markedly between extended and flush cases (Fig. 6c). The former shows three stagnant bands and the latter only one. Note also a correspondence to the V_{mag} patterns with a spot counterpart for each band. These stagnant bands and spots are emblematic of the disparity between the flush and extended case flow fields. The patterns persist across repeated measurements on the same day as well as different days (repeatability is considered in section 3.3).

Dynamic characteristics of the flow field are considered by plotting the RMS (root mean square) of the N/S and E/W velocity components (Fig. 7). A new color palette is introduced to clearly distinguish RMS data from the time-averaged velocities of the preceding plots. The extended case exhibits low intensity and relatively uniform N/S RMS while the flush case is less uniform with a distinct spot of high intensity centered over the east inlet. A clear disparity is also evident in the E/W component. The extended case has a concentrated band of relatively high RMS centered between the inlets while the flush case is far more diffuse with the region of highest intensity located above the west jet rather than centered between inlets. Like velocity, RMS exhibits a dichotomy between flush and extended geometries.

This collection of data suggests jet stability in the extended case and instability in the flush case. In the extended case, RMS is low everywhere except the interface between the jets where vortices mix and enhance turbulence. The high RMS region is narrow because the interface is stable, indicating the jets themselves are stable. Stability is also indicated by the three stagnant spots for V_{mag}, which are consistent with jets rising straight up from the inlets to spread across the lid in a symmetric fashion. Such a flow pattern would generate a stagnation point

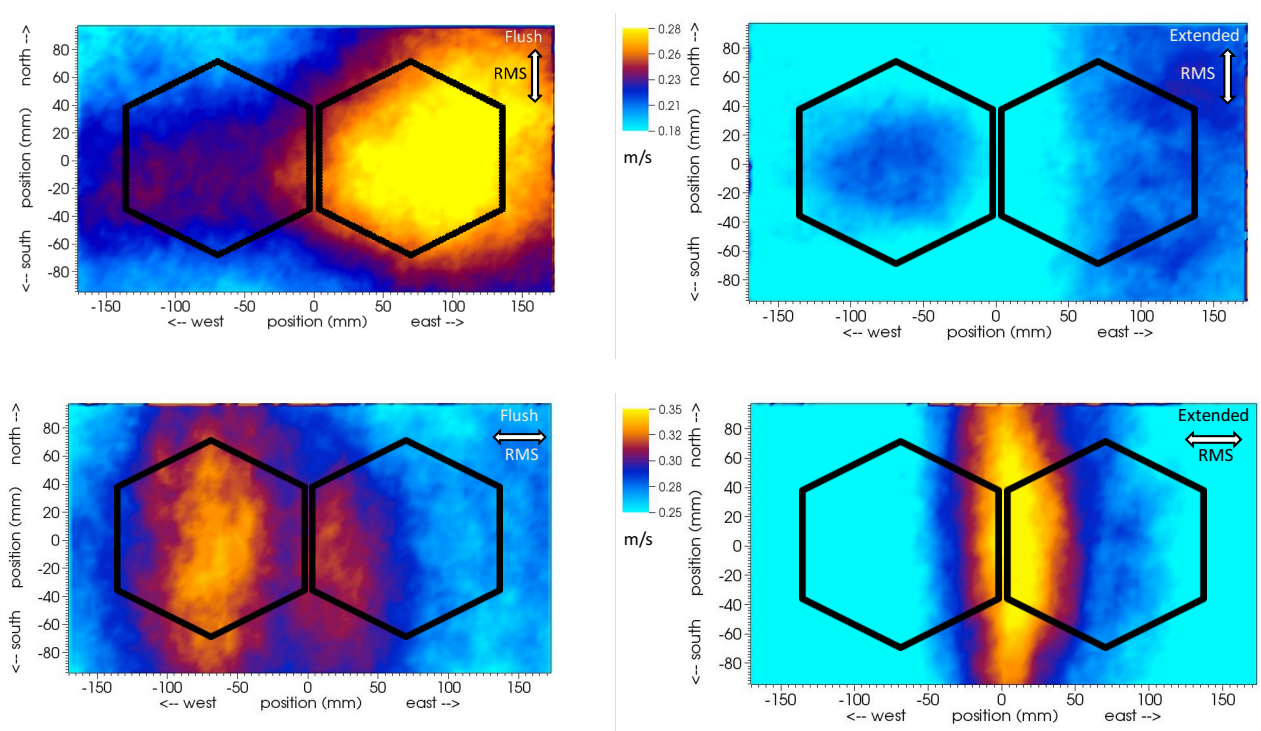

Fig. 7. RMS of velocity field 3 mm below lid for matched inlet flows at Reynolds 10000 and ambient temperature. Viewpoint from above tank looking down on lid. Top row: RMS of north/south component; bottom row: RMS of east/west component

directly above each inlet where the center of the jet impinges upon the lid and spreads radially outward. A third stagnant region would be present at the symmetry point where the wall flows from each jet meet. The same symmetries are responsible for the stagnant bands in Fig. 6c.

The flush case appears markedly less stable. The RMS data suggests the west jet moves primarily in the E/W direction while the east jet moves strongly in the N/S direction. The lone stagnation point is consistent with a single jet spreading across the lid, which could indicate jet coalescence en route to the lid or dominance of one jet while the other dissipates. Note again that the impingement flow field furnishes only an indirect indication of jet behavior. Later, simulation data is used to analyze the jets themselves.

The lid flow patterns presented above for Re=10000 have also been observed for Re=18000: three stagnant regions in the extended case and only one in the flush case (neither shown), supporting the notion that the jets are unstable in the flush case but stable with extensions. This result confirms that the stability dichotomy is not a special case at Reynolds 10000 with its particular combination of jet core length and distance to the lid. Inlet geometry is governing jet stability and the nature of the impingement flow field.

Frequency spectrums are another important consideration for thermal striping since the severity of thermal cycling and fatigue varies with the frequency of fluid temperature fluctuations. Frequency analysis is beyond the scope of this paper, however, as it focuses only on the flow pattern dichotomy associated with the inlet geometry change. The aim of the next two sections is to further establish that the stability dichotomy is a product of the inlet geometry rather than a chance combination of boundary conditions. This is an important consideration for code validation since boundary condition data is always accompanied by measurement uncertainties. It is therefore essential that the system response quantities under investigation are stable within the boundary condition envelop defined by measurement uncertainties. Otherwise apparent differences between simulation and experiment could be incorrectly attributed to modelling shortcomings.

3.2 PIV: mismatched isothermal jets

Companion tests were conducted to characterize the lid flow field for mismatched inlet flow rates. They again involved both the flush and extended configurations under isothermal conditions, but with one jet at Reynolds 10000 and the other slightly higher. Data is grouped into three sets: 1) east jet 2, 4, and 10% high; 2) west jet 2, 4, and 10% high; 3) matched jets for a comparison baseline. The purpose here is to exclude the possibility that the pattern switch occurs only for matched flow rates. Or, given flowmeter uncertainty (±0.8%), it occurs for mismatched flows mistakenly thought to be matched. Consistency in the lid flow pattern across a range of inlet flow conditions supports the case that the geometry switch is solely responsible for the observed changes in the impingement flow field. This supplementary data also demonstrates repeatability across two days of testing.

Tests are compared by plotting the E/W velocity component along the tank centerline. PIV data was sampled at the position shown by the dashed lines in Fig. 6c with an effective line width of 5.8 mm, the size of a PIV interrogation area. Results are presented in Fig. 8. Curves for mismatched flows are based on an average of two 1000-frame records while curves for matched flows use three records. Each curve includes records from two

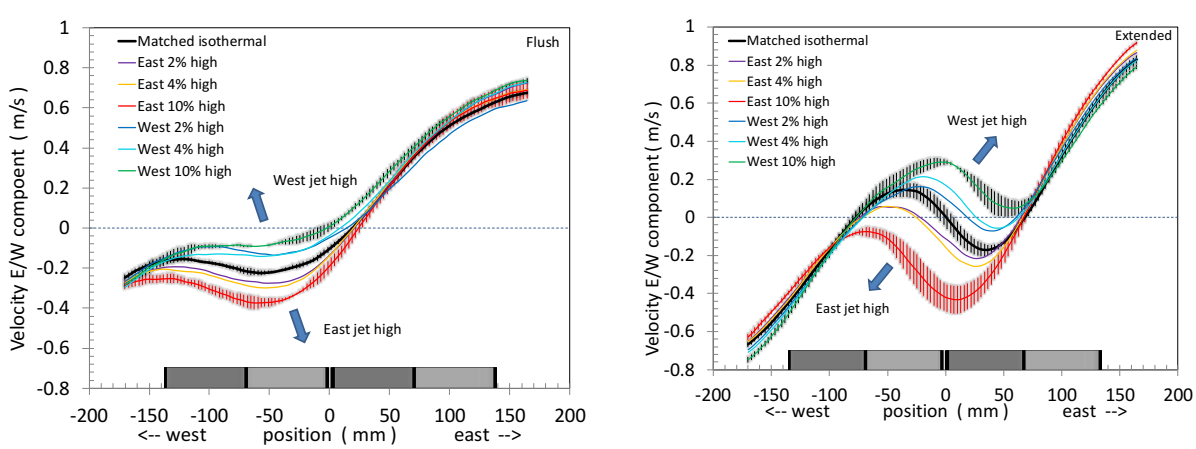

Fig. 8. Velocity below lid along tank centerline for mismatched isothermal flows near Re=10000 (location indicated by dotted line in fig. 6c); shaded regions represent ±σ based on two data records for mismatched cases and three cases for matched flow (for clarity plotted only for matched flow and ±10% mismatches). Extensions included as orientation aid.

different days. All records were logged at 5 Hz over 200s. The E/W component of velocity was chosen for comparison because the number of stagnant bands varies with inlet geometry. The V_{mag} data is similarly interesting, but line-sampled data is sensitive to the lateral locations of the stagnant regions, which may shift with flow rate and lead to much different curves even though the flow pattern remains essentially unchanged. E/W data is less sensitive to the sampling location since the stagnant bands extend across the entire data plane.

The curves in Fig. 8 exhibit a single zero crossing for the flush case and multiple crossings for the extended case. In each case curves maintain a distinctive shape across the entire range of flow rate mismatches. Zero crossings correspond to the black bands of Fig. 6c and, as shown earlier, tend to have a one-to-one correspondence with the V_{mag} stagnant spots. If we accept the premise that three stagnation points are an indirect indication of jet stability while a single stagnation point indicates instability, all the flush runs are unstable while the extended runs are stable, excepting the largest mismatches at 10%. Stability is seen to depend on inlet geometry even for flow mismatches well beyond the flow meter uncertainty of ±0.8%.

Error bands in the figures are represented by one standard deviation (σ). The sample population is only two 1000-frame records for the mismatched flows and three records for matched. Despite the small sample size, this is a useful indicator because measurements were recorded on two different days. It likely provides a more conservative gauge of uncertainty than more numerous records logged in succession on a single day. Standard deviation was computed as a function of position, showing that variability tends to be greatest near the inflection points. Despite the small number of samples and appreciable σ, the data suggests that flow mismatches up to 10% generate significant and repeatable shifts in the E/W velocity component along the lid centerline.

3.3 PIV: mismatched jet temperatures

A final set of tests with PIV explores the influence of mismatched jet temperatures on the lid flow field. Testing again involved both the flush and extended configurations near Reynolds 10000, but with a ΔT of 4, 2, or 0 ^{o}C at the inlets. The purpose is the same as that of the mismatched flow rate series, to confirm persistence of the flow patterns over an inlet mismatch range that exceeds measurement uncertainty (ΔT accuracy better than ±0.1 ^{o}C). In addition, these tests can reveal a threshold where buoyancy-induced flows begin to have a discernible influence on lid flow patterns, serving as a prelude to testing with higher ΔTs that are more characteristic of the thermal striping applications of interest.

It is not possible to precisely match both the inlet Reynolds number and mass flow rate at different temperatures. We elected to match jet mass flow rates at 1.25 kg/s with Re≈10000. The difference in inlet Reynolds numbers is then proportional to the difference in air viscosity, which is ~1% for ΔT=4 ^{o}C. This is not much larger than the flow meter uncertainty of ±0.8% and considerably less than the ±10% test range of the isothermal mismatch series.

Figure 9 shows the E/W velocity component below the lid for the temperature mismatch tests. Curves are again based on line samples of PIV data at the position marked by the dashed lines in Fig. 6c. Each curve is an average of three 1000-frame records logged consecutively at an interval of ~10 minutes. Testing was conducted over five consecutive days with nonstop air flow and each day devoted to a single ΔT setting. Every heater adjustment for a

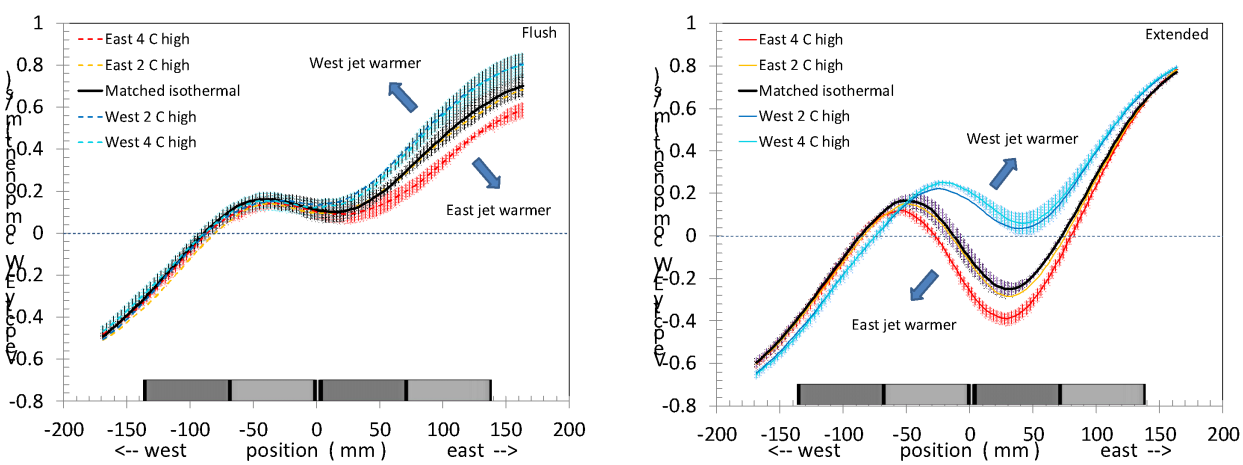

Fig. 9. Velocity below lid along tank centerline for mismatched inlet temperatures; Re≈10000.

new ΔT was followed by a ~24 hour settling time to establish a new thermal equilibrium. At each ΔT, the switch between the flush and extended configurations was made by opening the lid for < 2 min to insert or remove the extensions. The lid was then closed and the system given >1 hour to reestablish equilibrium, which is considered sufficient since the tank atmosphere is displaced at a rate of ~70 times/hour.

The temperature mismatch curves in Fig. 9 echo the velocity mismatch curves of Fig. 8. Curves associated with a particular geometry exhibit a distinct shape that is consistent across the ΔT test range. In both cases curves shift downward when the east jet is heated and upward when the west jet is heated. This is consistent with the isothermal flow mismatch tests: downward shifts for both east jet heated and east jet high; upward for both west jet heated and west jet high. The heated jet is seen to play the same role as the higher velocity jet in the isothermal tests.

Some shifts are as large as those of the isothermal flow mismatch tests though the Reynolds number mismatch is smaller. This is most notable in the extended case. If velocity mismatches alone drove changes in the impingement flow field, the effects of ±4 ^{o}C mismatches would be less than that seen for ±2% isothermal flow mismatches. But an inlet temperature difference of 4 ^{o}C shifts the curves nearly as much as ±10% in isothermal flow. This suggests that buoyancy forces are significant, and indeed mixed convection is indicated by the Richardson number $Ri= Gr/Re^2$, which is ~5 for ΔT=4 ^{o}C and tank height of 1 m.

In closing this section on PIV measurements, we acknowledge the significant disparity in velocity profiles for the two matched flush cases, plotted as heavy black lines in Figs. 8 and 9. Though these two test series were separated in time by 3 months, inlet boundary conditions were identical and so the profiles were expected to match, as they do in the extended case. Possibly the flush case is less repeatable simply because it is unstable. We must note, however, that there was a minor physical difference between the two test series: for the nonisothermal series, an array of steel wire, ϕ127 μm, was strung across the midplane in anticipation of a vertically-oriented DTS measurement plane that was not used here (see [36] for details). The wire had no apparent effect on the extended case, but might have influenced the flush case, again because it is unstable. Still, the anomaly does not invalidate earlier observations on general flow behavior and the influence of inlet geometry on jet stability.

3.4 Temperature field: mismatched jet temperatures

Air temperature was measured 3 mm below the lid with a DTS using the layout shown earlier in Fig. 3. The sensor and support wire were installed after completing all the PIV tests described above. Wire for the vertical array mentioned above was removed. Jet mass flows were again matched at Reynolds≈10000 and 1.25 kg/s with one jet heated above ambient. Tests were run with the east jet heated either 4 ^{o}C or 20 ^{o}C above the west jet, and the west jet heated either 4 ^{o}C or 20 ^{o}C above the east jet. All permutations were run for flush as well as extended configurations. The 4 ^{o}C case is considered here as a counterpart to the PIV data sets for the same ΔT, though for brevity only the heated east jet case is shown.

Figure 10 presents temperature and RMS contours for the flush and extended configurations. As with the PIV contours, the point of view is from above the tank looking down onto the lid. Note that the DTS data plane, at 0.48 x 0.83 m, is considerably larger than the PIV plane. Plots are based on 2000 scans logged at 4 Hz for a record length of ~8 minutes. Data was processed with a 30 mm gage length, the spatial resolution of each measurement along the fiber, for a total of 1355 independent measurements. This 30 mm gage was applied at 10 mm spacing in an oversampling mode that brings the total number of data points to 4067. Data was normalized by subtracting the mean temperature.

Figure 10 shows normalized temperature across the impingement flow field. As expected, the warmest regions are located above the heated inlet in both the flush and extended cases. But the two cases are not identical: temperature gradients are muted in the flush configuration with less distinct highs and lows, which is consistent with relatively good mixing driven by jet instabilities. In contrast, the thermal signature in the extended case is more distinct, as expected from a steady hot jet that does not mix well with the cold jet.

Disparities in mixing are more clearly indicated by the RMS contours in Fig. 10. Like the velocity RMS shown earlier, temperature RMS is diffuse in the flush case and concentrated along a narrow band in the extended case. Flush case jets are relatively well-mixed by the time flow reaches the lid and so flow field fluctuations cannot generate sizeable local temperature fluctuations. But steady jets in the extended case maintain a sharp gradient across the interface between warm and cold jets all the way to the lid. Consequently, the band of high turbulence drives an accompanying band of strong temperature variance.

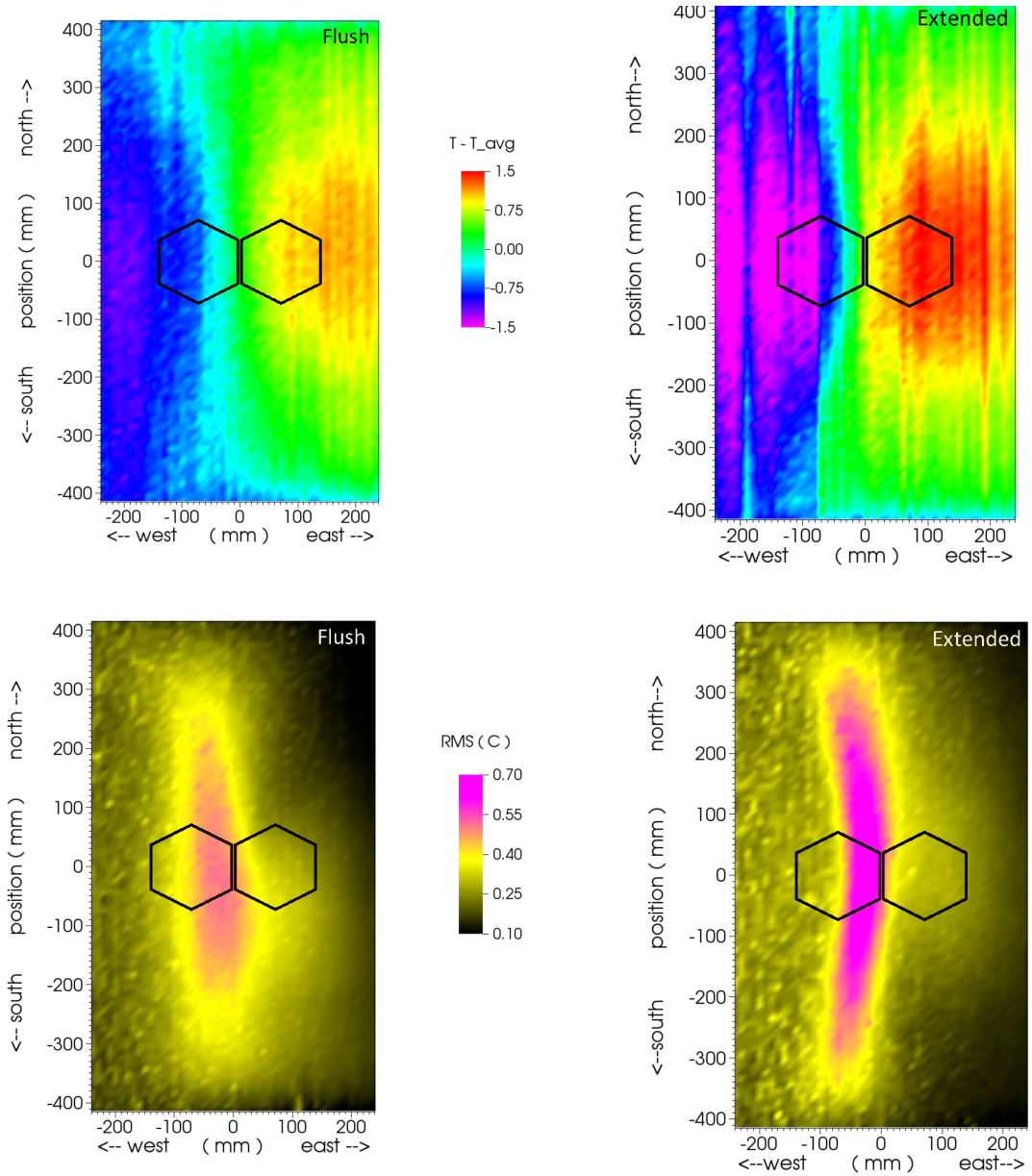

Fig. 10. Air temperature 3 mm below lid measured with DTS at Reynolds 10000 and east jet heated 4 °C above west jet. Top row: normalized temperature; bottom row: temperature RMS.

Measurement error for the DTS is difficult to quantify because the sensor is sensitive to strain as well as temperature. Accuracy of the ΔT shown here is estimated to be no better than ±0.2 °C. The vertical streaks in the temperature contours are due to a systematic positioning error that shifts adjacent sensor segments with respect to one other. The bias is ~5 mm and the resultant data offset generates streaks when interpolated to fill out the contour. Further details on error and repeatability for this particular setup are available in [37].

4. Simulations

4.1 Model description

The spectral element code Nek5000 was used to simulate the experiment for matched isothermal jets. Spectral elements methods are a class of higher-order methods in space. Polynomial functions of up to the 7th order on each element are employed to discretize the velocity field. Nek5000 has been extensively validated for a variety of flow conditions (see, e.g., [38]) and is massively parallel [39].

Simulations were performed on BLUE GENE/P with up to 30,000,000 collocations (60,000 element points using a Large Eddy Simulation approach (LES). In LES, large-scale turbulence is simulated while smaller scales are modeled. Since flow behavior at small scales is nearly universal, LES is more reliable than Reynolds Averaged Navier Stokes (RANS), which relies more on physical models. LES is also preferable to DNS (Direct Numerical Simulation) since it can be performed at more reasonable computational cost.

For the jet simulation presented here, contributions of small scales to the energy cascade are modeled through a local, element-based explicit cutoff filter in wavenumber space [40]. Energy is removed from the smallest simulated scales (high wavenumbers) thus mimicking the effect of smaller eddies. This procedure permits a coarser grid and therefore lower computational cost. Time advancement was carried out through a time-splitting characteristics-based technique [41] that permits larger time steps (CFL~2-3).

No-slip Dirichlet boundary conditions were applied at all walls while a turbulent outflow condition was applied at the outlets [42]. The inlet boundary conditions for the present case were originally treated by implementing cyclic boundary conditions between the inlets and cross-sections that are close to half the duct length [43]. However, it was found that flow at the boundary is better approximated as a uniform flow condition. Turbulent fluctuations were added using a divergence-free synthetic eddy method [44-46], which led to a significant improvement of the simulation results.

4.2 Results

Data analysis will focus on the lid area measured with PIV. Simulation results are presented in the same format as the experimental data to facilitate comparisons. Figure 11 shows contour plots of average velocity magnitude 3 mm below the lid for both the extended and flush cases. The former exhibits three stagnant regions and the latter only one, echoing the PIV data of Fig. 6a. Positioning of these regions is also duplicated with one centered between inlets and, in the extended case, another over each inlet. For the flush case, the stagnant region is larger in the simulation than experiment, but in both cases its core is ~15 mm east of center. These results demonstrate that Nek5000 is able to reproduce the observed dichotomy in impingement flow field that has been linked to the geometry change.

The extended case was computed for Re=10000, matching the experiment, with synthetic eddies at the inlet to mimic grid turbulence and account for mesh flow conditioners in the experiment. The flush case was computed for Re=8700 and cyclic inlet conditions, differing from the experiment because it is part of an early scoping study [43] conducted before settling on Re=10000 for the experiment. The flush case has not yet been run with

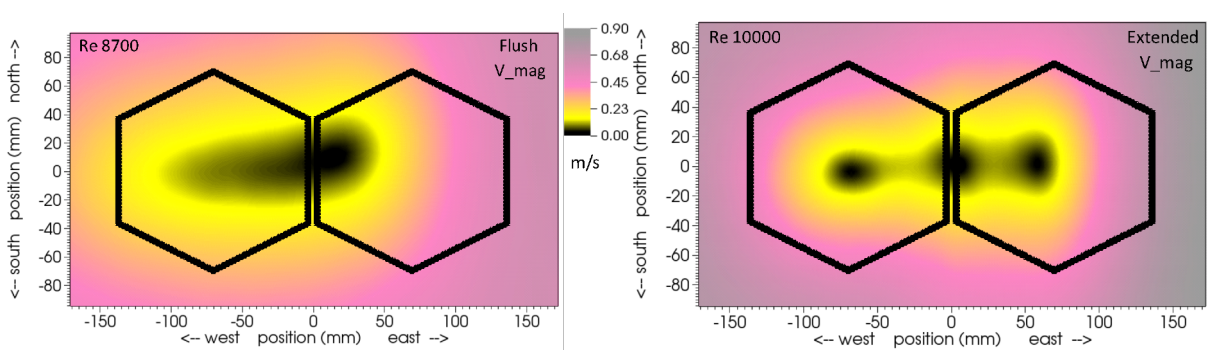

Fig. 11. Simulation results: lid flow field 3 mm below lid (counterpart to experimental data, Fig. 6a).

Re=10000 and synthetic eddy inlets because of the high computational cost. However, we will later demonstrate that the flow dichotomy of central interest here persists across an appreciable range of Reynolds numbers and inlet conditions. Thus the Re=8700 data set is considered adequate for this preliminary study.

Quantitative comparisons between experiment and simulations are presented in Fig. 12. The E/W velocity component was again chosen for scrutiny for the same reasons described earlier. Velocity is scaled by V_{bulk}, the average at the inlet, and position is scaled by D_{inlet}, the flat-to-flat distance of 136 mm for the hexagonal channels. Simulation data was sampled along the tank centerline at three distances from the lid including the 3 mm level of the PIV data. The curves for 2 and 4 mm parallel the ±1 mm uncertainty in light sheet position and provide a sense of its significance for these comparisons. It appears to be of marginal significance since the 2, 3, and 4 mm curves are closely spaced, indicating the impingement field at ~ 3 mm does not change abruptly with distance.

The image part with relationship ID rId39 was not found in the file.

Fig. 12. Velocity below lid along tank centerline for isothermal flow: simulation vs. experiment. Simulation data sampled at 2, 3, and 4 mm; experiment data plane at 3 mm ±1 mm.

The simulation curves in Fig. 12 mirror those of the experiment: a single zero crossing for the flush case and three crossings for the extended case. In the extended case, zero-crossings match the experiment within ~10 mm. Velocity magnitude is over-predicted by roughly 5% of V_{inlet} over the east inlet but is mostly within measurement uncertainty over the west inlet. In addition, all the extended case curves have the same essential shape across the entire data window.

The flush case is more problematic. Zero crossings of simulation and experiment coincide, but only for the PIV data of Fig. 8, plotted here, not for that of Fig. 9, which crosses at the west inlet instead of the midpoint between inlets. As noted earlier, the difference in the two data sets may be a consequence of instability and gradual shifts in the flow field over long time scales. A consistent representation of the average flow field might have been achieved through longer sampling timespans than those of this study. However, note again that the data of Fig. 9 is both consistent and logged over the substantial span of five days. Additional work is required to diagnose why 3-month repeatability was satisfactory for the extended case but poor for flush.

Figure 13 presents a collection of simulation curves for different Reynolds numbers and inlet conditions. Its purpose is to demonstrate persistence of the flow dichotomy across a range of inlet Reynolds numbers and differing inlet turbulence treatments, justifying the use of simulation data at Re=8700 to assess the flush case experiment run at Re=10000. Figure 13 includes two pairs of data for cyclic inlets, one at Re=8700 and the other at Re=20000. The fifth curve corresponds to the extended case at Re=10000 with synthetic eddies at the inlets, the same data used in earlier figures and best match to the experiment inlet boundary conditions. At Re=8700, the flush case exhibits a single zero crossing and the

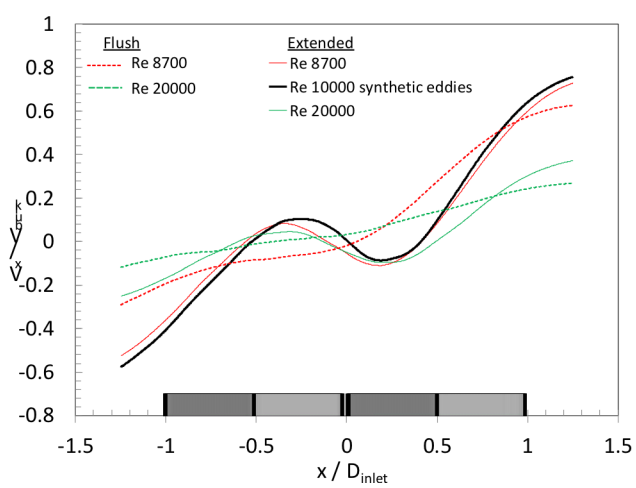

Fig. 13. Velocity below lid along tank centerline for isothermal flow (Nek5000); comparisons for differing inlet conditions.

extended three, as in the experiment at Re=10000. The pattern persists at Re=20000. It is next observed that the synthetic eddy curve for Re=10000 is a close match to Re=8700 with cyclic inlets, though with a slight lateral shift. This consistency despite varied inlet conditions suggests that a flush case simulation at Re=10000 with synthetic eddies would be similar to the Re=8700 case shown in Fig. 13. This collection of curves confirms, for the Reynolds number range examined here, the link between geometry and flow dichotomy as well as insensitivity to specifics of the inlet velocity profiles.

Finally, we note the relative stability of the zero crossing points in the extended case compared to flush. Roughly doubling the Reynolds number shifted the flush case zero crossing ~½ D_{inlet} while crossings remained nearly stationary in the extended case. This behavior may have a bearing on the observed difference in repeatability discussed in section 3.3.

4.3 Source of instability

It is interesting to consider a source for the stability dichotomy. Simulation data can suggest a possible mechanism through its view of the entire tank flow field. We first note that, along with the impingement flow fields, the jets themselves are discernibly different for the two geometries. This is illustrated by the snapshots in Fig. 14, which show instantaneous vertical velocity. Extended case jets are upright and reach the lid nearly intact while the flush case jets merge and fragment as they rise towards the lid. These snapshots are typical, though there is more variability in the flush case. Time-averaged data would tell the same story, but differences would be less distinct. Through these snapshots one can recognize how symmetries of the extended case generate three stagnant impingement regions while the asymmetric flush case does not.

The source of the instability is thought to lie in jet interactions with wall flows. In both geometries, flow reaches the lid with appreciable momentum rather than dissipating near the inlets. Flow subsequently spreads across the lid in all directions with a small fraction exiting directly through the outlet and a larger fraction impinging on the vertical walls. Wall flow proceeds downward, some reaching the bottom of the tank where it is driven by potential flow. In Fig. 14 the purple regions indicate downward flow, evident along the north, south, and east walls as well as the lower corners. These downward flow streams eventually reach the tank bottom and are directed away from the wall towards the inlets.

This flow pattern explains the relative importance of the extensions. In the flush case, flow crosses the bottom of the tank to converge with the base of each jet. Subsequent interactions may be strong enough to destabilize the jets, which is indicated indirectly through RMS of the lid velocity and temperature fields. Jet movement could in turn modulate bottom flow with feedback between the two setting up a repetitive process with long time scales (longer than the jet transit time to the lid). In contrast, extensions around the inlets may be protecting the jets from bottom flow, allowing them to remain stable. Further study is required to confirm this

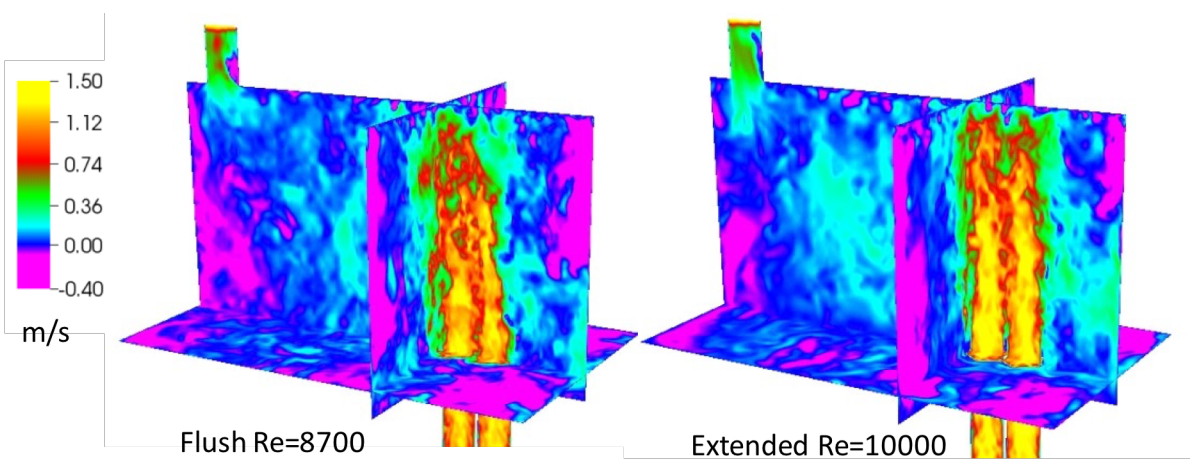

Fig. 14. Instantaneous vertical velocity (Nek5000) across midplane, 100 mm above base, and x=-136 (west edge of west inlet).

hypothesis.

5. Conclusion

We presented measurements of velocity and temperature across a wall impingement flow field driven by two jets, demonstrating that a small change in inlet geometry substantially altered both the flow and temperature fields. The impingement flow field varied with inlet configuration: three stagnant regions directly above the inlets for the extended case but only one for flush. In the extended case, flow field RMS is relatively high and concentrated in a narrow band between jets while it is more diffuse for the flush case. This collection of data provided an indirect indication of jet stability in the extended configuration and instability for flush.

A similar dichotomy was seen in measurements of air temperature across the impingement flow field during nonisothermal tests. Measurements were made at Re=10000 and inlet ΔT of 4 ^{o}C. For the flush case, temperature gradients across the impingement region are relatively small. This is consistent with enhanced mixing driven by instabilities that wash out the gradients before they reach the lid. The extended case exhibits more sharply defined hot and cold spots along with a narrow band of relatively high RMS similar to the band seen for velocity RMS. This is consistent with stable jets and inhibited mixing so that much of the inlet ΔT is maintained all the way to the lid.

Nek5000 was used to simulate the flow field in both the flush and extended cases under isothermal conditions. It reproduced the lid flow patterns seen in the PIV data, including the number of stagnant spots and their positions over the inlets. In quantitative comparisons, velocity magnitude matched well in the extended case but was less successful in the unstable flush case, which was not unexpected since the experiment itself exhibited appreciable variability in the flush case. Simulations corroborated experimental data indicating the flow dichotomy is not the result of a chance combination of jet core length and distance to the lid, but rather the difference in inlet geometry.

CFD simulations are sometimes tasked with predicting changes in flow and temperature fields associated with proposed design changes for a flow system. Reactor design simulations aimed at mitigating thermal striping are of this sort, and they would be expected to accurately predict interdependencies between geometry, flow field, and temperature field like those shown here. The clear flow dichotomy exhibited by this two-jet setup presents an unambiguous case to test CFD tools and their ability to predict subtle flow field changes driven by minor modifications in geometry in the context of thermal striping.

Acknowledgment

This work was supported by the U.S. Department of Energy, Office of Nuclear Energy. Data visualizations by VisIt; Bethel, E.W., Childs, H., Hansen, C., *High performance visualization: enabling extreme-scale scientific insight*, Chapman & Hall, 2012.

The submitted manuscript has been created by UChicago Argonne, LLC, Operator of Argonne National Laboratory ("Argonne"). Argonne, a U.S. Department of Energy Office of Science laboratory, is operated under Contract No. DE-AC02-06CH11357. The U.S. Government retains for itself, and others acting on its behalf, a paid-up nonexclusive, irrevocable worldwide license in said article to reproduce, prepare derivative works, distribute copies to the public, and perform publicly and display publicly, by or on behalf of the Government. The Department of Energy will provide public access to these results of federally sponsored research in accordance with the DOE Public Access Plan. http://energy.gov/downloads/doe-public-access-plan .

References

[1] J. Ahmad, J. Purbolaksono, L.C. Beng, Thermal fatigue and corrosion fatigue in heat recovery area side tubes, Eng. Fail. Anal. 17 (2010) 334-343.

[2] S. B. Lee, Thermal fatigue failure and design modification of a steam exhaust silencer, Eng. Fail. Anal. 2 4 (1995) 247-255.

[3] E. Blondet, C. Faidy, High cycle thermal fatigue in French PWR. Proceedings ICONE10 10th Int. Conf. Nucl. Eng., Arlington, VA April 14-18 (2002) paper 22762.

[4] M. Yetisir, Thermal fatigue in CANDU stations, Proc 17th Int. Conf. Nucl. Eng. (ICONE17), July 12-16 Brussels Belgium (2009).

[5] J.H. Kim, R.M. Roidt, A.F. Deardorff, Thermal stratification and reactor piping integrity, Nucl. Eng. Des. 139 (1993) 83-95.

[6] O. Gelineau, M. Sperandio, Ph. Martin, J.B. Ricard, L. Martin, A. Bougault, Thermal fluctuation problems encountered in LMFBRs, IAEA-IWGFR/90. In: Specialists' Meeting on Correlation Between Material Properties and Thermohydraulics Conditions in LMFBRs, Aix-en-Provence, France, November 22–24, (1994) 438-46.

[7] P. Chellapandi, K. Velusamy, Thermal hydraulic issues and challenges for current and new generation FBRs, Nucl. Eng. Des. 294 (2015) 202-225.

[8] J.C. Astegiano, Y. Lejeail, A. Rinijski, Specialists' meeting on correlation between material properties and thermohydraulics conditions in LMFRs, IWGFR/90 Aix-en-Provence, France, November (1994).

[9] T. Tenchine, S. Vandroux, V. Barthel, O. Cioni, Experimental and numerical studies on mixing jets for sodium cooled fast reactors, Nucl. Eng. Des. 263 (2013) 263-272.

[10] S. Moriya, I. Ohshima, Hydraulic similarity in the temperature fluctuations of non-isothermal coaxial jets. Nucl. Eng. Des. 120 (1990) 385-393.

[11] N. Kimura, H. Miyakoshi, H. Kamide, Experimental investigation on transfer characteristics of temperature fluctuation from liquid sodium to wall in parallel triple-jet. Int. J. Heat Mass Tran. 50 (2007) 2024–2036.

[12] J.P. Simoneau, H. Noé, B. Menant, Large Eddy simulation of sodium flow in a tee junction, comparison of temperature fluctuations with experiments. In: Proceedings of the 8th Nuclear Reactor Thermalhydraulics Conference (NURETH 8), Kyoto, Japan (1998).

[13] B. Rzezonka, H. Kastl, Stress and fatigue analysis of SNR-300 mixing devices, including optimizations and thermal shock tests on internal structures, Nucl. Eng. Des. 78 (1984) 69–78.

[14] R. Stieglitz, M. Daubner, A. Batta, C.H. Lefhalm, Turbulent heat mixing of a heavy liquid metal flow in the MEGAPIE target geometry- The heated jet experiment, Nucl. Eng. Des. 237 (2007) 1765-1785.

[15] N. Kimura, H. Ogawa, H. Kamide, Experimental study on fluid mixing phenomena in T-pipe junction with upstream elbow. Nucl. Eng. Des. (2010) 3055-3066.

[16] S.M. Hosseini, K. Yuki, H. Hashizume, Experimental investigation of flow field structure in mixing tee, J. Fluids Eng. 131 051103 (2009) 1-7.

[17] G. Pan, H. Meng, Experimental study of turbulent mixing in a tee mixer using PIV and PLIF, AIChE J. 47 12 (2001) 2653-2665.

[18] C. Walker, M. Simiano, R. Zboray, H. M. Prasser, Investigations on mixing phenomena in single-phase flow in a T-junction geometry, Nucl. Eng. Des. 239 (2009) 116-126.

[19] J. Kickhofel, V. Valori, H.M. Prasser, Turbulent penetration in T-junction branch lines with leakage flow. Nucl. Eng. Des. 276 (2014) 43-53.

[20] D. Lu, Q. Cao, J. Lv, Y. Xiao, Experimental study on three-dimensional temperature fluctuation caused by coaxial-jet flows, Nucl. Eng. Des. 243 (2012) 234-242.

[21] A. Tokuhiro, N. Kimura, An experimental investigation on thermal striping mixing phenomena of a vertical on-buoyant jet with two adjacent buoyant jets as measured by ultrasound Doppler velocimetry, Nucl. Eng. Des. 188 (1999) 49-73.

[22] H. Wang, S. Lee, Y. A. Hassan, A. E. Ruggles, Laser-Doppler measurements of the turbulent mixing of two rectangular water jets impinging on a stationary pool, Int. J. Heat Mass Tran. 92 (2016) 206-227.

[23] Y. Rathee, B.R. Vinoth, P.K. Panigrahi, K. Muralidhar, Imaging flow during impingement of differentially heated jets over a flat surface, Nucl. Eng. Des. 294 (2015) 1-15.

[24] M. Bovo and L. Davidson, Direct comparison of LES and experiment of a single-pulse impinging jet. Int. J. Heat Mass Transfer 88 102-110 (2015) http://dx.doi.org/10.1016/j.ijheatmasstransfer.2015.04.025.

[25] D. Violato, A. Ianiro, G. Cardone, F. Scarano, Three-dimensional vortex dynamics and convective heat transfer in circular and chevron impinging jets, Int. J. Heat Fluid Fl. 37 (2012) 22-36.

[26] T. Iwana, K. Suenaga, K. Shirai, Y. Kameya, M. Motosuke, S. Honami, Heat transfer and fluid flow characteristics of impinging jet using combined device with triangular tabs and synthetic jets, Exp. Therm. Fl. Sci. 68 (2015) 322-329.

[27] S.J. Yi, M. Kim, D. Kim, H.D. Kim, K.C. Kim, Transient temperature field and heat transfer measurement of oblique jet impingement by thermographic phosphor, Int. J. Heat Mass Transfer 102 (2016) 691-702. http://dx.doi.org/10.1016/j.ijheatmasstransfer.2016.06.062

[28] P. Grenson, O. Léon, P. Reulet, B. Aupoix, Investigtaion of an impinging heated jet for a small nozzle-to-plate distance and high Reynolds number: An extensive experimental approach. Int. J. Heat Mass Transfer 102 (2016) 801-815. http://dx.doi.org/10.1016/j.ijheatmasstransfer.2016.06.076

[29] X.M. Tan and J.Z. Zhang, Flow and heat transfer characteristics under synthetic jets impingement driven by piezoelectric actuator, Exp. Thermal Fluid Sci. 48 134-146 (2013) http://dx.doi.org/10.1016/j.expthermflusci.2013.02.016

[30] E. Fanning, T. Persoons, D.B. Murray, Heat transfer and flow characteristic of a pair of adjacent impinging synthetic jets, Int. J. Heat Fluid Fl. 54 (2015) 153-166.

[31] R. Mehryar, A. Giovannini, Twisted symmetry in multiple jets at low Reynolds number, Int. J. Therm. Sci. 77 (2014) 27-37.

[32] G. Grötzbach, Challenges in low-Prandtl number heat transfer simulation and modelling, Nucl. Eng. Des. 264 (2013) 41-55.

[33] S. Lomperski, N. Bremer, Max data report: jet stability versus inlet geometry, Argonne National Laboratory technical report ANL/NE-15/37 (2015).

[34] K.T. Christensen, The influence of peak-locking errors on turbulence statistics computed from PIV ensembles, Exp. Fluids 36 (2004) 484-497.

[35] D. Gifford, S. Kreger, A. Sang, M. Froggatt, R. Duncan, M. Wolfe, B. Soller, Swept-wavelength interferometric interrogation of fiber Rayleigh scatter for distributed sensing. Proc SPIE 6770 Fiber Optic Sens and Appl V Vol. 6770 (2007) F1-F9.

[36] S. Lomperski, C. Gerardi, W. D. Pointer, Distributed fiber optic temperature sensor mapping of a jet-mixing flow field, Exp. Fluids 56:55 DOI 10.1007/s00348-015-1918-6 (2015).

[37] S. Lomperski, N. Bremer, C. Gerardi, D. Lisowski, Performance assessment of a 50 m-long fiber optic distributed temperature sensor in a fluid dynamics experiment, Specialist Workshop Adv. Inst. Meas. Tech Nucl. Reactor Thermal Hydraulics, Livorno Italy June 15-17 (2016).

[38] A. Obabko, P. Fischer, O. Marin, E. Merzari, and W. D. Pointer, Verification and Validation of Nek5000 for T-junction, Matis, SIBERIA, and Max Experiments., Proceedings of the 16th International Topical Meeting on Nuclear Reactor thermal-hydraulics (NURETH-16), August 31st- September 4th 2015, Chicago, Illinois, USA .

[39] N. Offermans, O. Marin, M. Schanen, J. Gong, P. Fischer, P. Schlatter, A. Obabko, A. Peplinski, M. Hutchinson and E. Merzari, On the Strong Scaling of the Spectral Element Solver Nek5000 on Petascale Systems, EASC '16: Proceedings of the 4th International Conference on Exascale Applications and Software, 2016, April 26th -29th, Stockholm, Sweden.

[40] P.F. Fischer and J.S. Mullen, Filter-Based Stabilization of Spectral Element Methods",Comptes Rendus de l'Académie des sciences Paris, 332, Série I - Analyse numérique, 265-270 (2001).

[41] Y. Maday, A. Patera, E. Ronquist, An operator-integration-factor splitting method for time dependent problems: Application to incompressible fluid flow, J. Sci. Computing, pp. 263- 292 (1990).

[42] M. J. Kloker, H.F. Fasel, U. Konzelmann, Outflow boundary conditions for spatial Navier-Stokes simulations of transition boundary layers. AIAA Journal, 31(4):620-628, April 1993.

[43] E. Merzari, W.D. Pointer, A. Obabko, P. Fischer, On the numerical simulation of thermal striping in the upper plenum of a fast reactor. Proceedings of ICAPP '10, San Diego California, June 2010.

[44] N. Jarrin, S. Benhamadouche, D. Laurence, R. Prosser, A synthetic-eddy-method for generating inflow conditions for large-eddy simulation. Int. J. Heat Fluid Flow, 27(4):585-593, (2006). DOI: 10.1016/j.ijheatfluidflow.2006.02.006

[45] R. Poletto, Divergence-Free SEM (DF-SEM). PhD Thesis, University of Manchester, cfd.mace.manchester.ac.uk/twiki/pub/Main/TsfpPaper/tsfp template.pdf (2011).

[46] G.R. Tabor, Baba Ahmadi, M., Inlet conditions for large eddy simulation: A review. Computers & Fluids, 39(2010):553-567, October 2009.